The Radiative Budgets of a Tropical Mesoscale Convective System During the EMEX-STEP-AMEX Experiment 2. Model Results

Takmeng Wong, Graeme L. Stephens, and Paul W. Stackhouse, Jr.

Department of Atmospheric Science, Colorado State University, Fort Collins

Francisco P. J. Valero

NASA AMES Research Center, Moffett Field, California

This paper describes calculations of the spatial and temporal variation of the radiation budget of a tropical mesoscale convective system (MCS). A combination of cloud model simulations, radiation model simulations, and analyses of observations obtained during the Equatorial Mesoscale Experiment (EMEX), the Stratosphere-Troposphere Exchange Program (STEP), and the Australian Monsoon Experiment (AMEX) are used to obtain these heating rates. The two-dimensional version of the Colorado State University regional atmospheric modeling system is used to simulate a tropical MCS that occurred during EMEX mission 9 on February 2, 1987. The simulation is shown to broadly agree with the observations reported in a related paper. The spatial radiative heating distributions derived from a two-stream radiative transfer model corresponding to the mature stage of the simulated cloud system indicate that significant horizontal inhomogeneities exist. According to the model results the effects of the MCS are to (1) increase in the infrared emission to the surface and to decrease in the net infrared energy loss from the atmosphere relative to the clear sky emission and (2) change the transmission of solar flux to the surface, the shortwave albedo of the atmosphere, and the solar absorption in the atmosphere. The results show how the MCS significantly reduces the solar flux to the surface relative to the clear sky values and that the largest reduction occurs under the convective portions of the mature MCS. (3) The MCS creates a total (solar plus infrared) radiative warming in the atmosphere relative to the surrounding clear sky. The value of this total heating is governed by both infrared and solar absorption. Vertical profiles of this heating show the dominance of infrared cooling near cloud top and infrared heating inside and near cloud base. The shortwave heating rate can also be as large as the infrared cooling near the cloud top region of the tropical MCS, especially at a local noon. (4) The temporal changes in radiation profiles also demonstrate how the MCS modulates the radiation budget of the atmosphere. Specifically, the total radiation energy loss of the entire two-dimensional domain of the model atmosphere decreases and eventually becomes positive as the cloud system decays, becomes a stratiform in nature, and fills the domain. This change in the column divergence of flux translates into a total column radiative heating rate of approximately 1.7 K/d (relative to the clear sky radiative cooling rate). The solar component of this domain heating tends to be concentrated in the upper troposphere, whereas the infrared component of the heating is spread over the lower and middle troposphere. These results also show how tropical mesoscale cloud system provides an effective radiative heat source for the tropical atmosphere.

1. Introduction

A number of studies have pointed to the importance of radiative processes both on tropical mesoscale convective systems (MCSs) and on the large-scale tropical circulation and perhaps even controlling the climate regimes in which tropical MCSs exist [*Ramanathan and Collins*, 1991]. The contribution of radiation to the total diabatic heating profile is thought to be significant in the mesoscale region due to radiative flux divergence in the presence of the extensive upper tropospheric cloud shields [*Webster and Stephens*, 1980]. *Ackerman et al.* [1988] have further demonstrated that radiative heating of the order of 20 to 30 K/day is expected in tropical anvil clouds. This radiative heating rate may be a source of buoyant turbulence in the anvils [*Lilly*, 1988] and perhaps produces significant mesoscale circula-

tions. The modeling study of *Chen and Cotton* [1988] also shows how radiative heating and cooling modulates circulation patterns in the mesoscale region by destabilizing the stratiform cloud region. *Dudhia* [1989] proposes that radiative heating is an important forcing of the vertical motion in the upper troposphere. In addition to in-cloud radiative heating, the infrared radiative clear air cooling can further aid the convection by continuously destabilizing the troposphere. *Gray and Jacobson* [1977] propose that a secondary circulation may be induced by the differences between clear air and cloudy air radiative heating. *Stuhlmann and Smith* [1988a, b] further find that cloud-generated radiative heating can affect the general circulation of the atmosphere by altering the generation of the available potential energy.

Although significant progress has been made in addressing the effects of radiative heating associated with these tropical MCSs, a full understanding of the spatial and temporal variation of this radiative heating is not yet available. This is partially due to lack of detailed spatial and temporal in-cloud radiation measurements and also to the simplified assumptions used in early radiative transfer models

of these cloud systems. This paper describes a study that seeks to use a combination of cloud model simulations, radiation model simulations, analyses of observations obtained during the Equatorial Mesoscale Experiment (EMEX), the Stratosphere-Troposphere Exchange Program (STEP), and the Australian Monsoon Experiment (AMEX), and comparisons with other published studies of similar tropical MCSs, to estimate the spatial distribution of this radiative heating and to investigate the change of this heating through the life cycle of the cloud system. The observation data based on EMEX-STEP-AMEX experiments have been described by *Wong et.al.* [1992; hereafter referred to as part 1].

Sections 2 and 3 present, respectively, a short outline of the numerical cloud and radiation models and the initial conditions used in the numerical simulation. Sections 4 and 5 present the model results which demonstrate the spatial characteristics of the total (solar plus infrared) radiative heating/budget during the mature phase of the tropical MCS and how the total radiative heating/budget of the atmosphere can change significantly during the evolution of the tropical MCS. Section 6 summarizes the results of the study and presents the conclusions.

2. DESCRIPTION OF THE NUMERICAL MODEL

A hybrid cloud-radiation diagnostic model is developed in this study to calculate the radiation profiles within a simulated tropical MCS. The approach is to use a dynamical cloud model to provide the time evolution of cloud thermodynamic and bulk hydrometeor fields and incorporate these fields into a detailed two-stream multiband radiation model to calculate the radiative budgets of the MCS. This hybrid diagnostic approach is not completely closed as the radiation budget derived from the detailed two-stream radiation model does not interact with the rest of the cloud model physics. The dynamical cloud model does, however, utilize a simpler broadband radiation scheme [*Chen and Cotton, 1983; Stephens*, 1978] to crudely account for this cloud-radiation interaction. A more detailed investigation of these couplings is the subject of a future study by the authors. Another limitation of the present approach is that the radiation model requires a transformation from the mixing ratio values of the various bulk hydrometeor species provided by the cloud model to the more explicit information about the radiation scattering parameters used in the two-stream radiative transfer model. This transformation is described in more detail below.

2.1. Dynamical Cloud Model

The numerical cloud model used in this study is the Colorado State University regional atmospheric modeling system (CSU-RAMS). As described by *Cotton and Tripoli* [1978], *Tripoli and Cotton* [1980, 1982], and *Cotton et al.* [1982, 1986], this model is nonhydrostatic, fully compressible, and includes a full set of dynamical, thermodynamical, and microphysical equations for water and ice phase particles. The model predicts all three components of the velocity, the ice-liquid potential temperature [*Tripoli and Cotton*, 1981], the Exner function, and the mixing ratios of different bulk hydrometeor species including total water, rainwater, ice crystal, graupel, and aggregates. The dry air density, cloud water mixing ratio, and potential tempera-

ture are diagnostic variables in the model. The size distribution of these bulk hydrometeor quantities are prescribed in the model. Parameterization of sub-grid-scale turbulence is also contained in the model using a simple first-order closure scheme in which eddy exchange coefficients for heat and momentum are calculated as a function of fluid deformation and Richardson number.

For this study, the cloud model is formulated on a two-dimensional (2-D) grid of 500×32 points which represents a domain of 500 km in the horizontal and 21 km in the vertical. Previous works on the tropical MCSs (i.e., *Xu and Krueger* [1992], *Nicholls and Weissbluth*, [1988], and *Tao et al.* [1987]) have demonstrated the validity of 2-D cloud simulations for studying the physical processes associated with these cloud systems. The horizontal resolution chosen to resolve convection in the tropical MCS is 1km [e.g. *Nicholls*, 1987] and the vertical grid is stretched slowly from 400 m near the surface to 1 km at top of the model to minimize gravity wave refraction due to rapid changes in vertical spacing [*Nicholls*, 1987]. A weak dissipative layer is applied to the highest 8 km of the domain to reduce reflection from the upper rigid walls. The kinematic and thermodynamic/microphysical variables in the model are set up on a staggered grid system [*Tripoli and Cotton*, 1982]. Rigid walls are used as vertical boundaries. Frictional effects are neglected at the bottom boundary but fluxes of latent and sensible heat from the ocean surface are included in the model by specifying a constant temperature and moisture gradient. The lateral boundaries include a mesoscale compensating region (MCR) [*Tripoli and Cotton*, 1982] to provide a large-scale balance adjustment of circulation generated within the interior of the model domain. The *Klemp and Lilly* [1978] radiation boundary condition is also applied as the lateral boundaries of the fine mesh to allow propagation of gravity waves through the fine mesh/MCR walls and to minimize the reflection of these gravity waves back to the model domain. The cloud model is initialized at approximately 0516 LST on February 3, 1987 at latitude 9°S and longitude 139°E using sounding data obtained from Darwin, Australia, and integrated forward in time for 6 hours with a 10-s time step. A more complete description of the model initialization is given in section 3.

2.2. A Diagnostic Two-Stream Radiation Model

The two-stream plane parallel multiband radiative transfer model developed by *Stackhouse and Stephens* [1991] is used in this study to diagnose the upward and downward fluxes for the relevant solar (0.28 μm - 3.8 μm) and infrared (3.8 μm - 200.0 μm) wavelength ranges. This radiation model is formulated in such a way as to treat the physical processes such as absorption and scattering by both molecules and particles in a consistent way. The optical properties of molecules and particles that characterize absorption and scattering processes in the model are the single-scattering albedo, the asymmetry factor, and the attenuation coefficient. The particulate optical properties (i.e., optical properties of the ice and water species) are determined using Mie solutions assuming equivalent diameter spheres from the particle size spectrum, the gaseous absorption is calculated using the k-distribution method for H_2O, CO_2, and O_3 in both the solar and the infrared wavelengths, as well as O_2 absorption in the solar spectrum. Parameteri-

zations of Rayleigh scatter [Paltridge and Platt, 1976] and e-type absorption in the 8- to 13- μm window region [Kneizys et al., 1980] are also included.

For this study, the total number of bands in the radiative transfer model is greatly reduced from the original version to just 24 bands (shown in Table 1) to model the absorption spectra of the atmospheric gases. Specifically, solar absorption by O_3 for wavelengths less than 0.68 μm is treated by dividing the spectrum into three bands using the O_3 cross sections for each band. For wavelengths greater than 0.687 μm, the k-distribution method is applied for 11 bands and 10 bands for infrared wavelengths greater than 3.8 μm. The optical paths associated with each gas are computed using the simple pressure-temperature scaling parameterization with scaling constants as given for each gas by Chou and Arking [1980, 1981], Chou and Peng [1983], and Chou [1984, 1990]. The spectral bands and the scalings used are summarized in Tables 2a and 2b.

The cloud particle optical properties employed in this study (i.e., attenuation coefficient, single-scatter albedo, and

TABLE 1a. Infrared Spectral Bandwidths of Abosrbing Gases

Band	Infrafred Spectral Bandwidth, cm^{-1}	Absorber
1	20 - 340	H_2O
2	340 - 540	H_2O
3	540 - 620	H_2O + CO_2
4	620 - 720	H_2O + CO_2
5	720 - 800	H_2O + CO_2
6	800 - 980	H_2O
7	980 - 1100	H_2O + O_3
8	1100 - 1380	H_2O
9	1380 - 1900	H_2O
10	1900 - 2620	H_2O

TABLE 1b. Solar Spectral Bandwidths of Absorbing Gases

Band	Solar Specral Bandwidth, cm^{-1}	Absorber
1	2600 - 3300	H_2O
2	3300 - 4000	H_2O + CO_2
3	4000 - 4600	H_2O
4	4600 - 5300	H_2O + CO_2
5	5300 - 6000	H_2O
6	6000 - 7000	H_2O + CO_2
7	7000 - 12850	H_2O
8	12850 - 13150	H_2O + O_2
9	13150 - 14300	H_2O
10	14300 - 14450	H_2O + O_2
11	14450 - 14550	O_2
12	14550 - 25000	O_3
13	25000 - 31746	O_3
14	31746 - 35710	O_3

asymmetry factor) for both ice and water species are derived from Mie theory assuming equivalent diameter spheres as specified by the particle size spectrum. The size distributions used in the Mie calculations correspond to those of the prescribed bulk hydrometeor species in the dynamical cloud model (with the exception of cloud water and ice crystal) and are representative of the typical size distributions found in a tropical convective system for the five classes of hydrometeor species of cloud water, rain, ice crystal, graupel, and aggregate crystals. These distributions are summarized in Table 3. The total concentration of each species is diagnosed from both the prescribed size distributions and the mixing ratio predicted by the cloud model. Since the actual ice crystal size distribution is perhaps less well known, we chose to represent this variable using ice crystal size spectrum data obtained from the aircraft measurements during the FIRE IFO experiment [Stackhouse and Stephens, 1991; Heymsfield et al., 1990]. A modified gamma size distribution is taken to represent cloud droplet distributions in the Mie calculations and the parameters of this size distribution are also contained in Table 3. The cloud optical properties derived from these Mie calculations are further modified to account for the molecular absorption using the k-distribution data, as described by Stackhouse and Stephens [1991].

3. INITIAL CONDITIONS

The initial conditions for the cloud model were based on both the observational data discussed in part 1 and the sounding data from Darwin, Australia (1700 UTC), on February 2, 1987 (shown in Figure 1a). The temperature profile closely follows a moist adiabat and the dew point temperature indicates the presence of a warm moist surface air layer with a drier region above. Surface temperature and mixing ratio values exceeded 27° C and 20 g/kg, respectively. The tropopause is located at about 100 mbar with a minimum temperature of -83° C. This sounding is similar to the Global Atlantic Tropical Experiment (GATE) sounding used previously by Nicholls [1987] in his simulation of tropical squall lines.

The wind profile, defined relative to the propagation direction of the tropical MCS which, in turn, is based on cloud motion estimation from satellite data, is given in Figure 1b. This profile indicates a shallow system-relative easterly flow near the surface, strong westerlies above 900 mbar, and strong easterly flow above about 200 mbar. The layer of westerlies has a bimodal structure with the major peak at 550 mbar and a secondary peak at 250 mbar. Vertical wind shear in the lower 2 km of the sounding is large with a difference of 8 m/s across this layer. Strong vertical shear also exists between 200 and 250 mbar. The maximum westerly wind speed is about 14 m/s at 550 mbar and the maximum easterly wind speed is observed to be 18 m/s at 100 mbar.

TABLE 2a. Infrared Scaling Parameters

Gas	Bandwidth, cm^{-1}	P_{ref} mbar	n	T_{ref} K	m	$R(T_{ref}-40K,T_{ref})$	$R(T_{ref}+40K,T_{ref})$
H_2O centers	20 - 340, 1380 - 1900	275	1.00	225	0.0	0.90	1.16
H_2O wings	340 - 1380, 1900 - 3000	550	1.00	256	0.0	0.58	1.78
CO_2 centers	620 - 720	30	0.85	240	0.0	0.74	0.44
CO_2 wings	540 - 620, 720 - 800	300	0.50	240	0.0	0.51	2.03
O_3 centers	980 - 1100	100	1.00	240	1.0	...	...

TABLE 2b. Solar Scaling Parameters

Gas	P_{ref} mbar	n	T_{ref} K	m
H_2O	300	0.80	240	0.0
CO_2	300	0.80	240	0.0
O_2	500	0.80	240	0.0
O_3	...	...	...	...

Following *Nicholls* [1987], the convection in this simulation is initialized by perturbing a horizontally homogeneous environment prescribed by the data illustrated in Figures 1a and 1b. This perturbation, which is used to represent the temperature and moisture jump across the leading edge of the tropical system, has the form of a warm moist bubble with a small cooling rate upwind of the bubble. The size of the warm bubble is approximately 10 km in width, 3 km in height, 1° C warmer, and 4 g/kg moister than the environment. A cooling rate of 0.006° C/s is applied to an area 15 km in width and 3 km in height, for the first 20 min of the model simulation time. As *Nicholls* [1987] notes, this type of initialization quickly produces a long-lasting tropical MCS.

Other information needed to initialize the cloud model includes the specification of certain cloud microphysical parameters (such as the mean radius of hydrometeors and the cloud condensation nuclei concentration). The cloud model in this study includes parameterizations for cloud water, rainwater, ice crystals, graupel, and aggregates. Microphysical information used in the initialization is derived from GATE data. In this regard we follow *Nicholls* [1987] and use a cloud condensation nuclei concentration of 100 cm^{-3} and characteristic mean radii of 0.027 cm and 0.05 cm for rainwater and graupel, respectively. These parameter values are also consistent with the results of *Carlson and Prospero* [1977], *Leary and Houze* [1979], and *Houze et al.* [1979].

We initialize the cloud model at approximately 0516 LST and integrate the model forward in time for 6 hours ending at 1116 LST. This particular time integration period is chosen in our study so that we can examine the effects of both the variation in solar insolation and the evolution of the cloud cluster on the total (solar plus infrared) radiative budgets of the cloud cluster system. The model results are described in detail below.

4. MODEL SIMULATIONS

The simulated MCS quickly develops after the initialization attains a mature stage after 3 hours with a maximum vertical velocity of 4 m/s and slowly decays after that time. Figures 2a and 2b respectively, contrast the fields of the total cloud hydrometeors at 3 hours and 6 hours into the

TABLE 3. Size Distribution for Different Water Species

Water Species	Size Distribution	D_{mean}, cm
Cloud	Modified Gamma	0.0003
Rain	Marshall-Palmer	0.0540
Ice Crystal	FIRE Ice	0.0168
Aggregate	Marshall-Palmer	0.3300
Graupel	Marshall-Palmer	0.1000

FIRE, First International Satellite Cloud Climatology Project Regional Experiment.

simulation, respectively. At 3 hours (Figure 2a) the MCS consists of a leading convective-stratiform region which is approximately 180-200 km in extent with a trailing anvil cloud extending from the front to the rear of the system. Areas of higher concentrations of cloud hydrometeors also exist at the rear of the stratiform region. The convective area in the leading portion of the MCS has a rearward sloping structure and seems to merge into the stratiform area. The rearward slope in the simulation has an angle of about 16.5° and is similar to the observed structure of EMEX 9 cloud structure (specifically, the 17° rearward sloping angle noted in Figure 5a of part 1). The merging of the convective line into a stratiform precipitation area is also observed during EMEX 9 in which the convective portion of the system was imbedded in the broader area of stratiform precipitation. The horizontal scale of the convective region extends approximately 40-50 km and the stratiform-anvil region has a horizontal scale of 300-350 km. The vertical extent of the simulated system is 15 to 17 km. Both the horizontal and the vertical scales agree well with the observed scales of the EMEX 9 cloud system noted earlier from infrared satellite imagery and also noted previously from composite WP-3 airborne Doppler radar data [*Houze et al.*, 1988; *Webster and Houze*, 1991]. Overall, this simulated cloud system fits very well with the description of a typical mesoscale cloud cluster proposed by *Houze* [1989]. The MCS at 6 hours (Figure 2b) is characterized as a weak stratiform cloud system with an extensive anvil region that fills almost the entire model domain.

The lifetime of the simulated system is about 6 hours compared to 12 hours observed from the satellite observation. This disagreement may be due partly to the fact that we did not attempt to include the previously mentioned cloud cluster merger in the simulation. The satellite observations discussed in part 1 indicated how this merger seemed to strengthen the EMEX 9 cloud cluster and presumably to
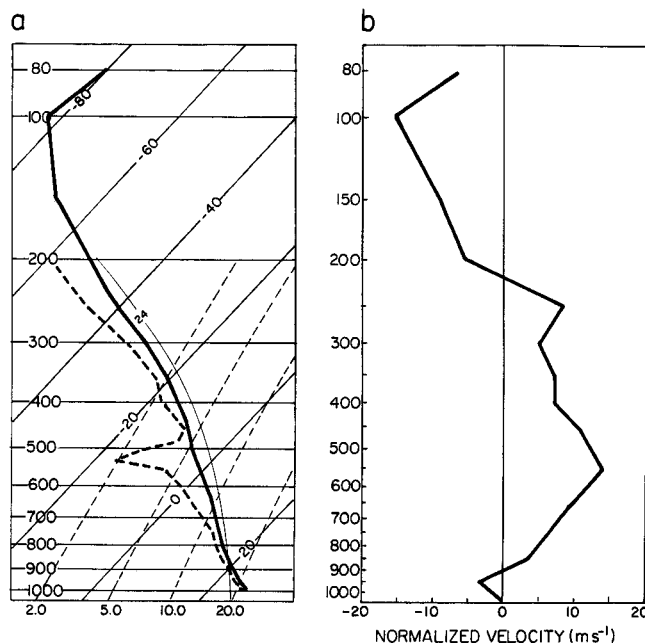

Fig. 1. The Darwin's sounding profile: (a) temperature (solid) and dew point (dashed) and (b) horizontal wind normal to the direction of EMEX 9 cloud cluster, at 1700 UTC on Febraury 2, 1987.

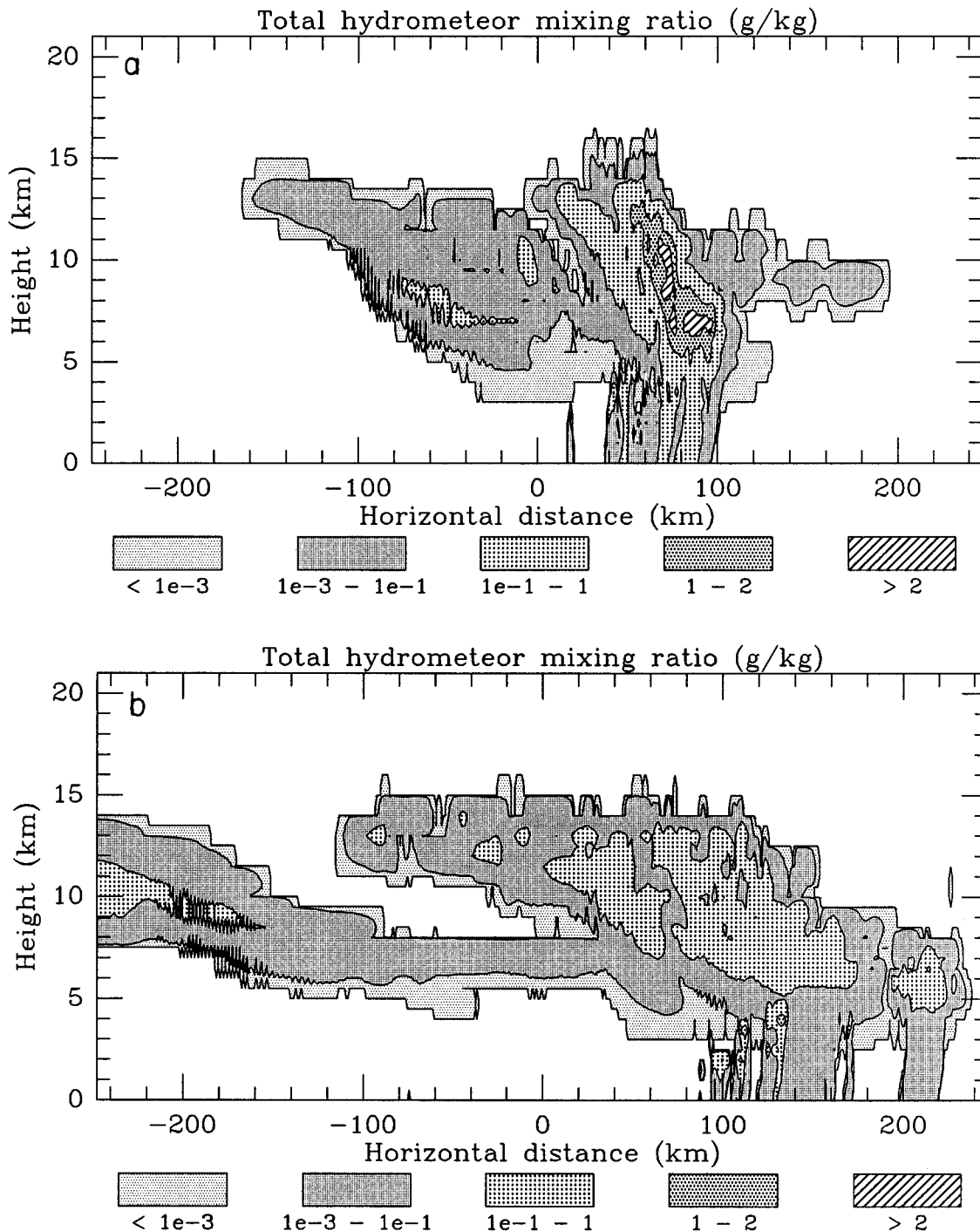## Total hydrometeor mixing ratio (g/kg)

Fig. 2. Simulated two-dimensional field (X-Z cross section) of total hydrometeor mixing ratio (g/kg) as predicted by the Colorado State University regional atmospheric modeling system (CSU-RAMS) cloud model at (a) 3 hours and at (b) 6 hours.

maintain the system. Our simulated system moves eastward (from left to right) at an approximate speed of 9 m/s compared to 12 m/s observed from satellite data. The slower speed of the simulated system may also be indicative of an inadequate horizontal resolution of our model which cannot capture updrafts and downdrafts on scales smaller than 1 km. The detail structures of the simulated EMEX 9 cloud cluster fields at 3 hours into the simulation are discussed in more detail below.

4.1. Microphysical Fields

A more detailed breakdown of the microphysical fields 3 hours into the simulation is presented in Figure 3a and 3b. Figure 3a shows the vertical cross section of total ice mixing ratio which is the combination of ice crystal, graupel, and aggregate mixing ratios, and Figure 3b shows the total liquid water mixing ratio derived from a combination of both precipitation and cloud water. According to these diagrams,

Total ice water mixing ratio (g/kg)
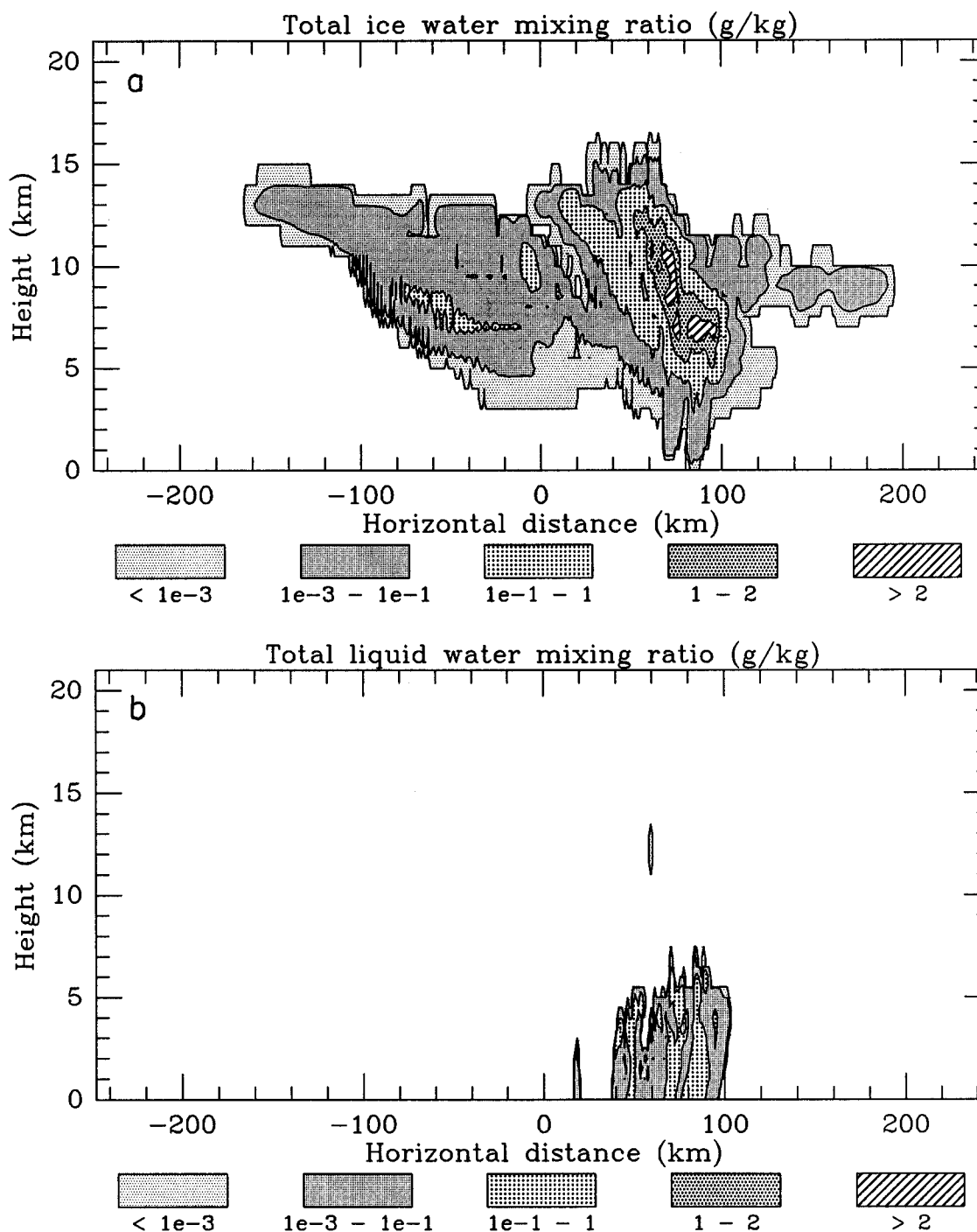

Total liquid water mixing ratio (g/kg)

Fig. 3. Simulated two-dimensional (X-Z cross section) mixing ratio fields (g/kg) of (a) total ice water species and (b) total liquid water species as predicted by the CSU-RAMS cloud model at 3 hours.

most of the total liquid water (cloud plus rainwater) and the graupel are found in the convective region. While cells of cloud water scatter across in the convective region below 10 km, the rainwater and the graupel are clustered in the convective line. The largest values of graupel mixing ratio are located between 5 km and 10 km in the convective region. The rainwater mixing ratio spreads across the convective region and some part of the stratiform area below 7 km. Regions of large rainwater mixing ratios are also predicted at the surface in the convective region. Ice crystals and

aggregates in the simulated cloud system are located above the freezing level (above 5 km). Ice crystals are mostly found between cloud top and 8 km and aggregates are located at lower levels in the stratiform region, and high mixing ratios of both ice crystals and aggregates are also found in the MCS region. At a height above 10 km the mixing ratio of these two species begins to tilt backward with height and merges into the stratiform region. The thin anvils located to the front and to the rear of the system are mostly ice crystals, whereas the stratiform region is composed of mostly

aggregates below 7 km. Above this level, ice crystals are the main form of water species.

4.2. Dynamical and Thermodynamical Fields

The vertical cross sections of horizontal and vertical velocity predicted at 3 hours are shown in Figure 4. The circulation consists of a low-level inflow into the leading convection, an low-level outflow behind this convection, an upper level outflow in front, and an upper level outflow behind the system. These upper level outflows to the front and rear of the system help carry cloud particles away from the convec-

tive cells and produce the stratiform anvil clouds in front of and behind the main MCS. The low-level easterly wind ahead of the system continuously feeds the convective region of the cloud cluster with warm moist surface air. This result is consistent with our synoptic analysis of part 1 which suggests the low-level surface northwesterly flow in the vicinity of the premonsoon trough area helped feed the cloud cluster with warm, moist surface equatorial air. The simulated circulation is also consistent with cloud model simulations described by *Moncrieff and Miller* [1976] and *Thorpe et al.* [1982] as well as those observed by *Chong et al.* [1987]. The convective region consists of small cells of upward and down-
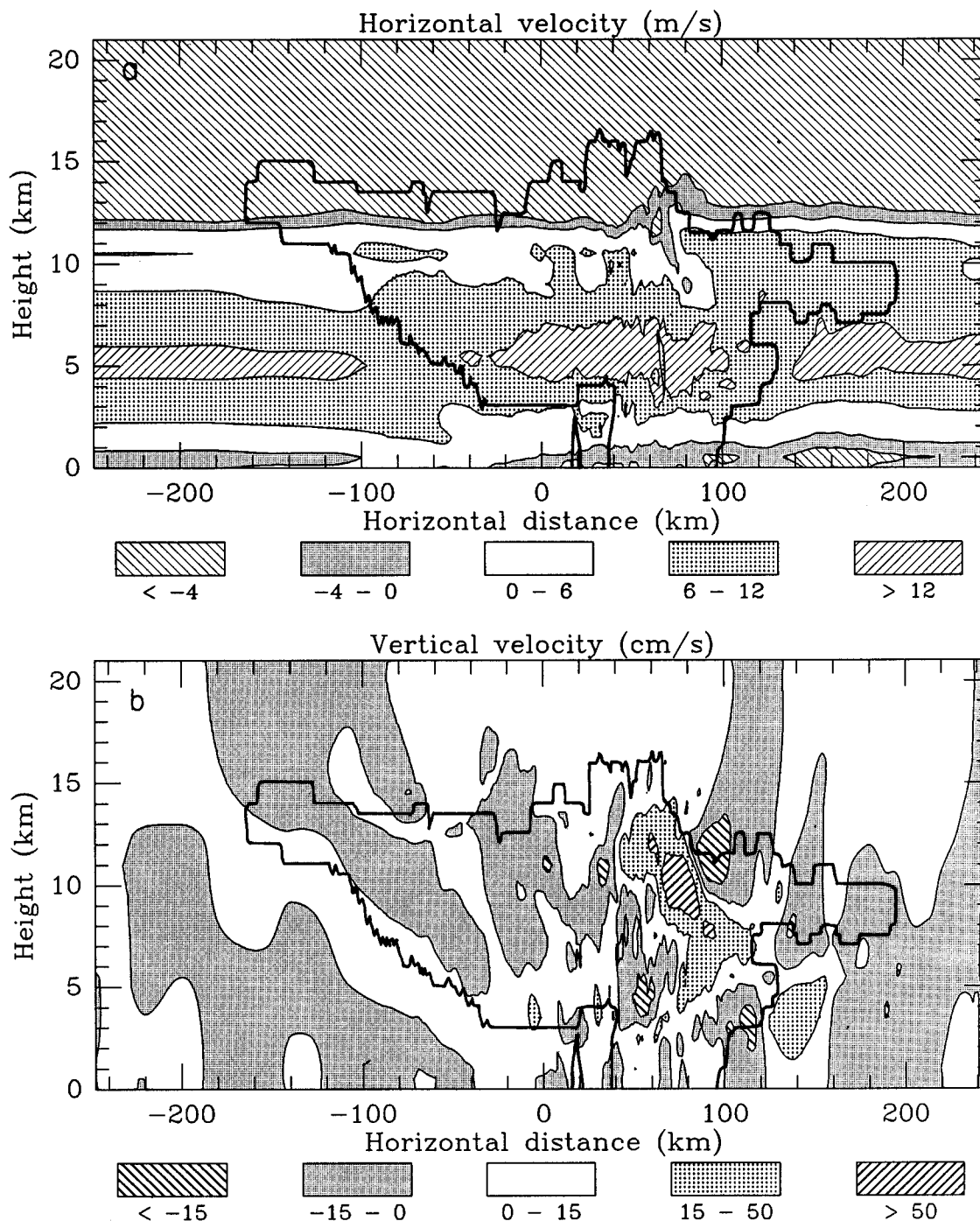

Fig. 4. Simulated two-dimensional (X-Z cross section) fields of (a) horizontal wind (m/s) and (b) vertical motion (cm/s) as given by the CSU-RAMS cloud model at 3 hours.

ward motion with horizontal scales of about 1-5 km. The convective updrafts have a rearward sloping structure with maximum upward velocity at upper troposphere (about 10 km). Strong low-level convective downdrafts are found in the region just ahead of the intense upper level updrafts due to the rearward sloping nature of the convection. These simulated convective scale vertical motions are consistent with the observed vertical motion structure of EMEX 9, as noted in part 1. In front of the cloud system, broad-scale downward compensating air motion is observed. While the leading convective region is comprised of strong upward mo-

tion, a complicated pattern of downward and upward motions exists in the stratiform regions as well as rear descending inflow jet which is also a feature of this region. This rear descending inflow jet, which is similar to some of the observed features of EMEX 9 in Figure 7 of part 1, tilts downward with height and collides with the surface creating an enhanced region of vertical motion in an area 80 km behind the main convection. Downward/upward motions are also found inside/below the cloud deck in the anvil region. This weak upward motion below the cloud deck in some part of the anvil region is responsible for the fine structures in
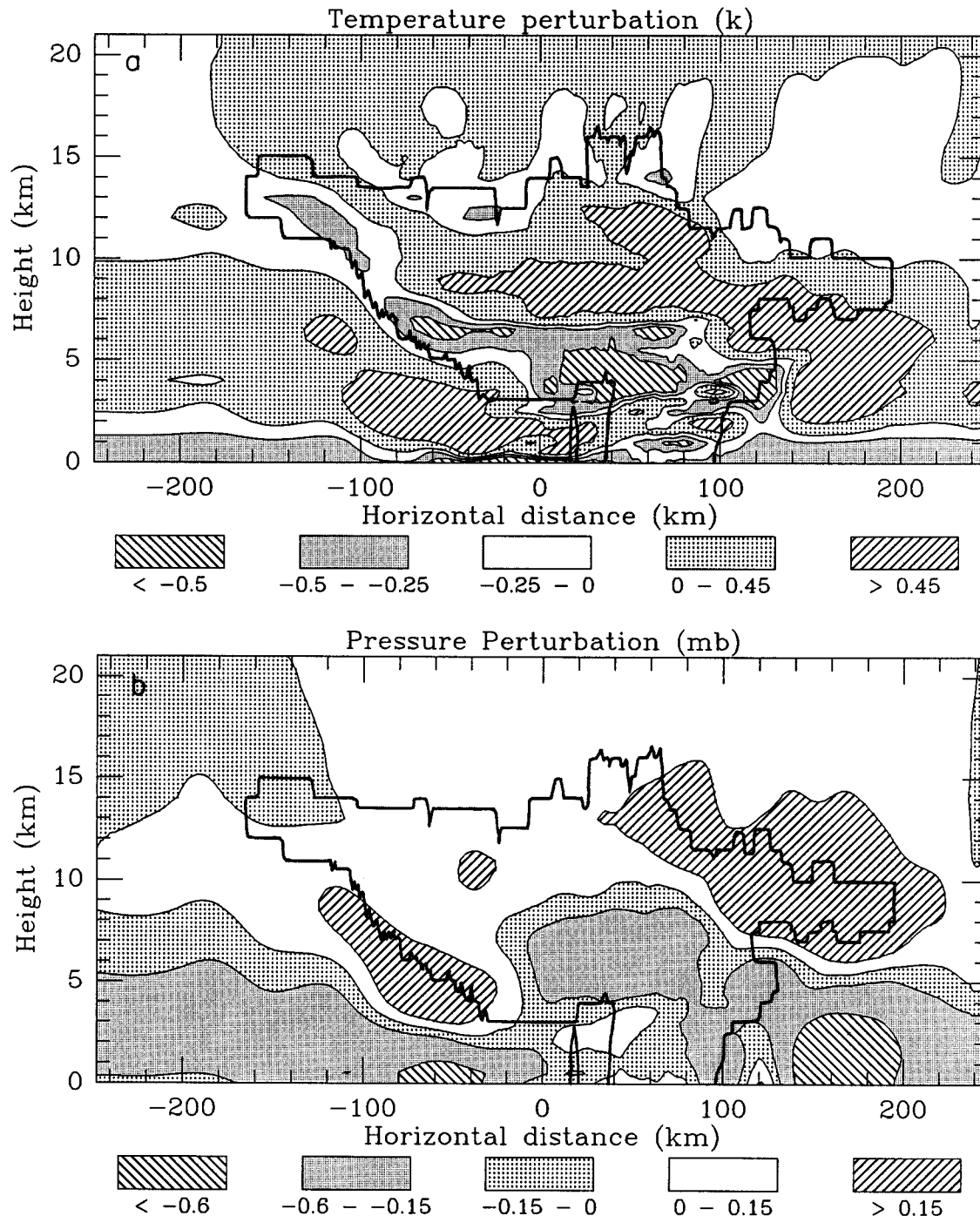

Fig. 5. Simulated two-dimensional (X-Z cross section) fields of (a) temperature perturbation (K) and (b) pressure perturbation (mbar) as given by the CSU-RAMS cloud model at 3 hours.

cloud hydrometeor fields in this region. The strong horizontal wind shear near the cloud top at 200 mbar is a product of the wind profile used to initialize the model and is maintained throughout the entire simulation.

The temperature and pressure perturbation fields after 3 hours are given in Figure 5. The temperature perturbation field (Figure 5a) indicates a cooling at the lower levels with a cold pool behind the leading edge of the cloud boundary. This low-level cold pool is also evident in the observed insitu low-level aircraft (F-27) data of the EMEX 9 system [*Webster and Houze*, 1991]. Warm air perturbations occur near the main updraft between 1 and 4 km above the surface and the effects of subsidence warming ahead of the system are

also evident. Significant warming/cooling is also located in the cloud above/below 7 km. This warm air perturbation above 7 km in the convective region is the cause of the maximum updrafts observed in the upper troposphere in this area. A tongue of relatively warm air exists behind the system and extends downward to the surface. The pressure perturbation field (Figure 5b) at the surface shows a meso-high in the vicinity of the convection and a mesolow in the region to the rear of the system. These surface features are common to mid-latitude and tropical mesoscale convective cloud systems (i.e., *Johnson and Hamilton* [1988] and others) and seem to be well simulated by the cloud model.
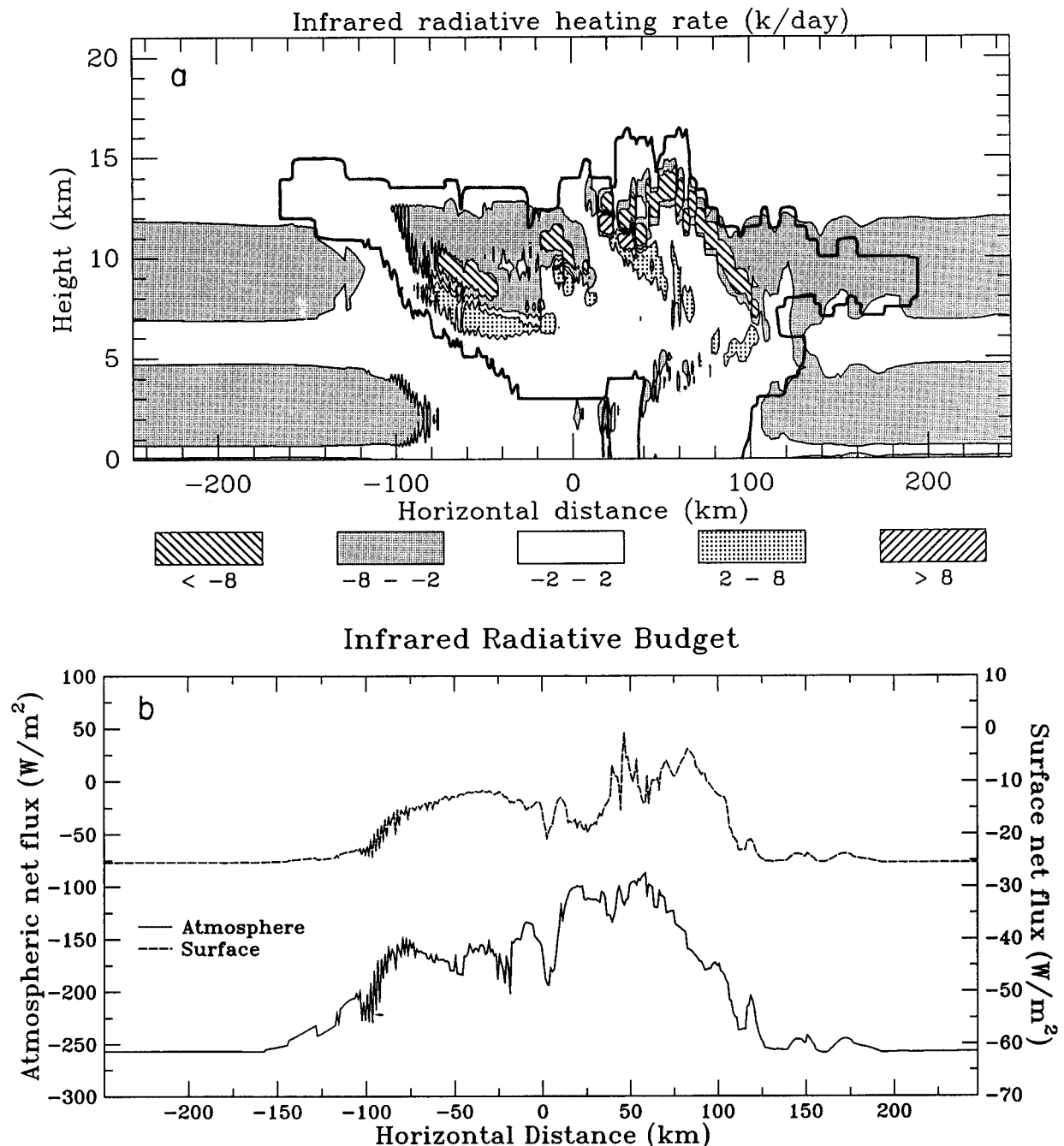

Fig. 6.(a) Two-dimensional (X-Z) cross section of infrared radiative heating field (K/d) and (b) infrared radiative budgets (W/m²) as a function of the domain horizontal distance for the surface (dashed line and right label) and the atmosphere (solid line and left label) as diagnosed by the two-stream radiation model at 3 hours.

5. RADIATIVE BUDGET SIMULATIONS

The radiation simulations now described demonstrate how the total (solar plus infrared) radiation budget of the atmosphere is significantly perturbed by the presence of the MCS.

5.1. Spatial Structures of the Cloud Radiation Budget

The simulated infrared (IR) radiative heating rates and infrared radiative energy budgets at 3 hours (0816 LST) for the EMEX 9 cloud cluster are shown in Figures 6a and

6b, respectively. The vertical cross section of the simulated infrared radiative heating rates highlight the dominance of infrared cooling in both the clear sky and at the cloud top where the deepest cloud circulation occurs. Since the infrared optical depths are directly related to the total hydrometeor mixing ratio fields, one expects a high correlation between the spatial structure of the simulated infrared heating/cooling rates in Figure 6a and the spatial structure of the total hydrometeor mixing ratios in Figure 2a. This strong correlation is evident in our model results. The strong infrared cooling extends well into the upper portions of the
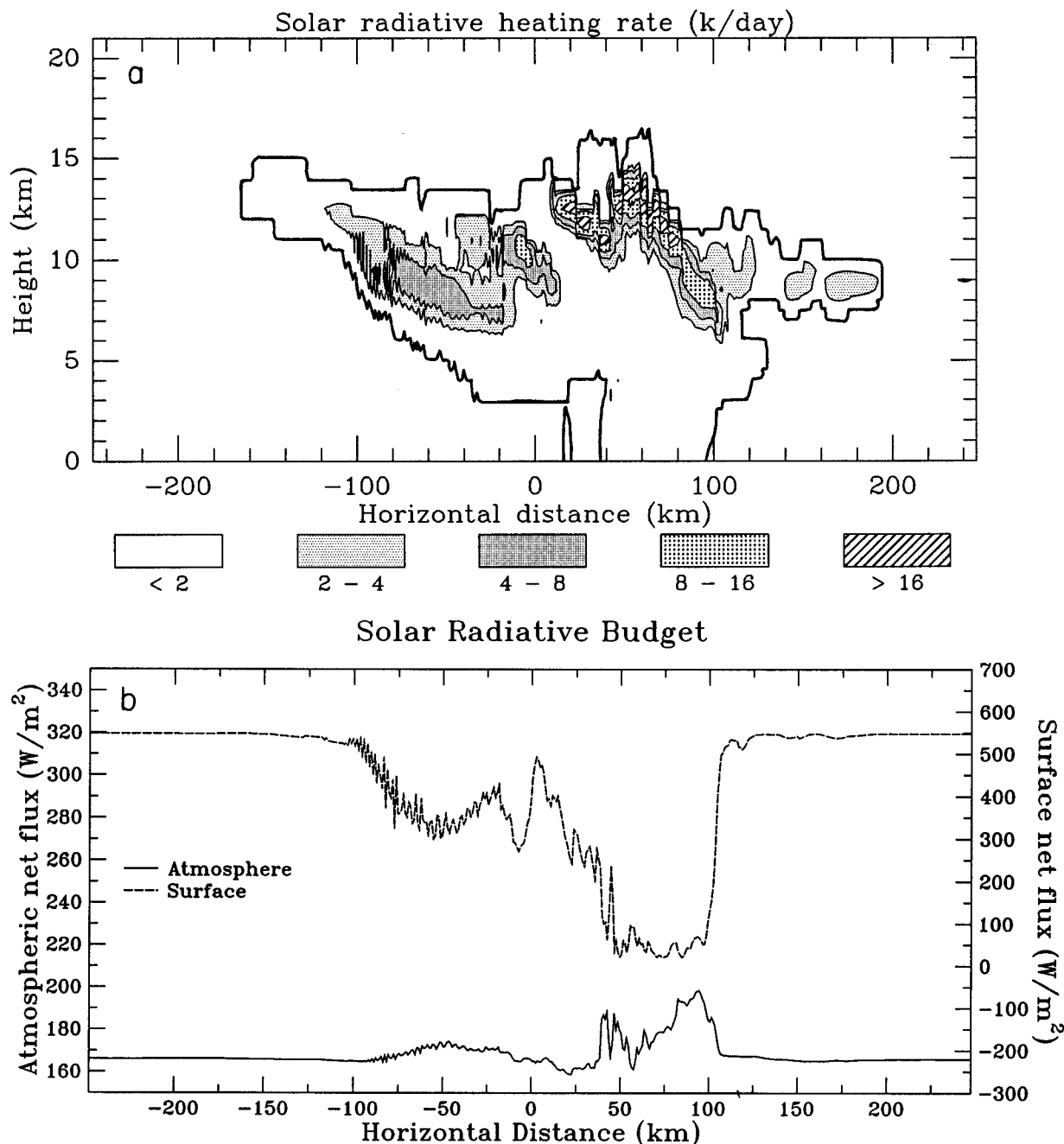

Fig. 7. (a) Two dimensional (X-Z) cross section of shortwave radiative heating field (K/d), (b) shortwave radiative budgets (W/m^2) as a function of the domain horizontal distance for the surface (dashed line and right label) and the atmosphere (solid line and left label), and (c) shortwave transmission (%) to the surface (dotted) shortwave albedo (%) at top of the atmosphere (solid) and shortwave absorpion (%) in the atmosphere (dashed) as a function of the domain horizontal distance, as diagnosed by the two-stream radiation model at 3 hours. The convective, stratiform, and thin anvil regions are highlighted in A, B, and C, respectively, in (c).
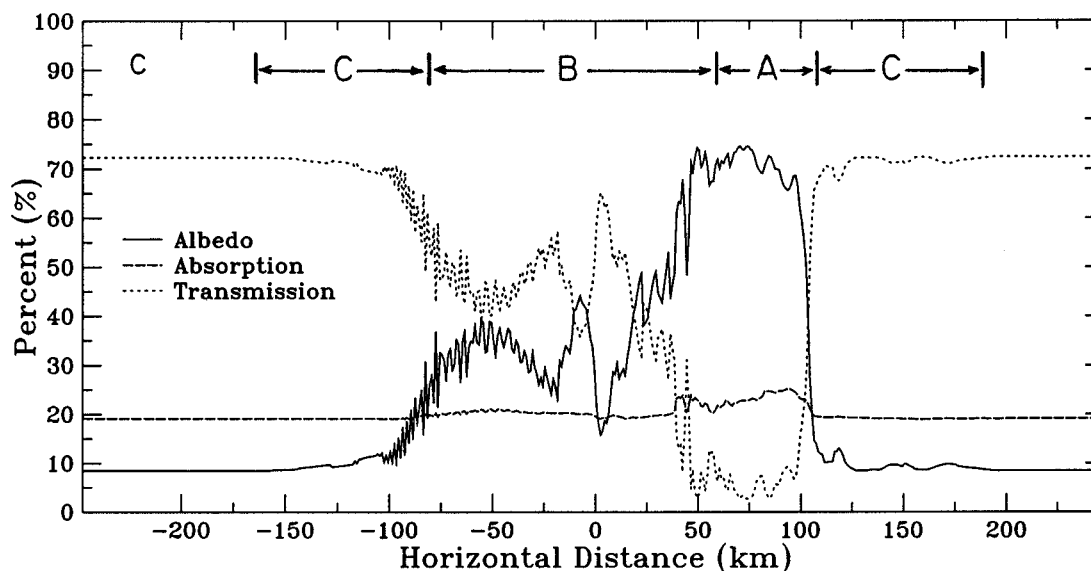
Shortwave Radiative Budget

Fig. 7. (continued)

anvil. Infrared heating exists inside and near the cloud base area in both the main convective- stratiform region and at the base of the thin anvil cloud. The maximum IR radiative heating and cooling rates found in this simulated radiation field are 36.5 and 32.3 K/d, respectively. Significant horizontal variability in the radiative heating/cooling across the cloud domain is also apparent in Figure 6a. The net infrared fluxes at the surface and the net convergence of infrared flux (the difference between the net infrared fluxes at the top of the atmosphere and at the surface) are presented as a function of horizontal position in Figure 6b. The results presented here show how the cloud system acts to increase the flux to the surface and also how the net tropospheric infrared flux is decreased relatively to the clear sky net flux. While the increase in the net IR flux at the surface is about 15 to 30 W/m^2, the decrease in outgoing IR flux at the top of the model atmosphere is as large as 150 W/m^2 in some areas of the cloud and is indicative of the significant greenhouse effect of these clouds, as described by *Stephens and Greenwald* [1991] and others. The maximum simulated upward brightness temperature values, which are calculated from the upward spectral infrared fluxes at top of the model atmosphere, are -76° C and -55° C for the convective and the stratiform regions, respectively. These values are similar to those observed from GMS satellite, as given in Figure 3 of part 1.

The simulated shortwave energy budget and radiative heating rates at 3 hours (0816 LST) for the EMEX 9 cloud cluster are shown in Figures 7a, 7b, and 7c. These shortwave radiation fields are presented in a manner similar to the IR results. The vertical cross section of the solar heating rates (shown in Figure 7a), calculated assuming insolation corresponding to 0816 LST, indicates a substantial in-cloud solar heating near the cloud top at this time with a maximum value of the simulated solar heating in Figure 7a is about 33 K/d. The spatial structures of the simulated solar heating rates in Figure 7a again correlate to the spatial structure of the total hydrometeor fields. Solar heating penetrates much

farther down into the cloud than the infrared cloud top cooling. The shortwave energy budget given in Figure 7b shows the variation of net shortwave flux at the surface and the net convergence of shortwave radiation in the model atmosphere across the model domain. One striking feature between the solar and the infrared energy budget of this cloud cluster is evident in comparing Figure 6b and Figure 7b. While the cloud cluster seems to have a smaller effect (about 30 W/m^2) on the net shortwave energy budget of the atmosphere, the surface shortwave energy budget shows a significant modification due to the cloud system. The infrared radiative effects, by contrast, are larger in the atmosphere than at the surface. The shortwave albedo at the top of the atmosphere, the solar transmission at the surface and the fractional absorption within the atmosphere are also presented in Figure 7c. Comparison between Figure 7b and Figure 7c shows that the downward flux at the surface is generally less than 150 W/m^2 beneath the most opaque convective and stratiform cloud regions, whereas significantly more solar radiation is transmitted through the optically thin anvil regions. Figure 7b and 7c also indicate that the shortwave absorption in the atmosphere is only slightly increased (up to 5 % or less) by the presence of the tropical cloud cluster at this time (0816 LST). However, the presence of clouds significantly alters the vertical disposition of this heating. The shortwave heating increases in the upper troposphere at cloud top but is reduced significantly below cloud base, especially at the surface. The upward reflected shortwave flux has a maximum above the convective and stratiform regions of the MCS. According to Figure 7c the shortwave albedo, absorption, and transmission are approximately 70-75%, 25%, and 5-10%, respectively, for the convective region (highlighted as region A); 25-70%, 21%, and 9-54%, respectively, for the stratiform region (region B); and 9-25%, 19%, and 56-72%, respectively, for the thin anvil region (region C). The transmission values quoted for the stratiform region are similar to the average transmission value deduced from the WP-3 aircraft measurements (i.e., Figure 8 of part 1) during the

later stage of the observed EMEX 9 cloud cluster system.

Figures 8a and 8b combine the results of the previous diagrams and present the vertical cross sections of the total (solar plus infrared) radiative heating rate, the horizontal distribution of total flux at the surface, and the total flux convergence in the atmosphere. These diagrams demonstrate the combined effects of the infrared and solar radiative transfer processes. The total radiative heating rates show a continuous cloud top cooling as well as cloud base heating. While the total radiative cooling in the convective region is confined only to an area near the upper levels of the cloud, the total radiative heating in this region penetrates much

deeper into the cloud cluster system. The maximum value of total radiative heating and cooling in Figure 8a is 39.9 K/d and 15.4 K/d, respectively. Furthermore, this figure also serves to stress the significant horizontal inhomogeneity in the total radiative heating rates spanning across the entire cloud system. A comparison of Figure 8b with Figures 6b and 7b shows that the largest effect of clouds at 0818 LST on the solar radiation budget appears as a significant reduction in the flux at the surface relative to the clear sky values. The latter can be identified with the clear sky values defined at the edge of the model domain. The influence of cloud on the longwave fluxes largely occurs in the atmo-
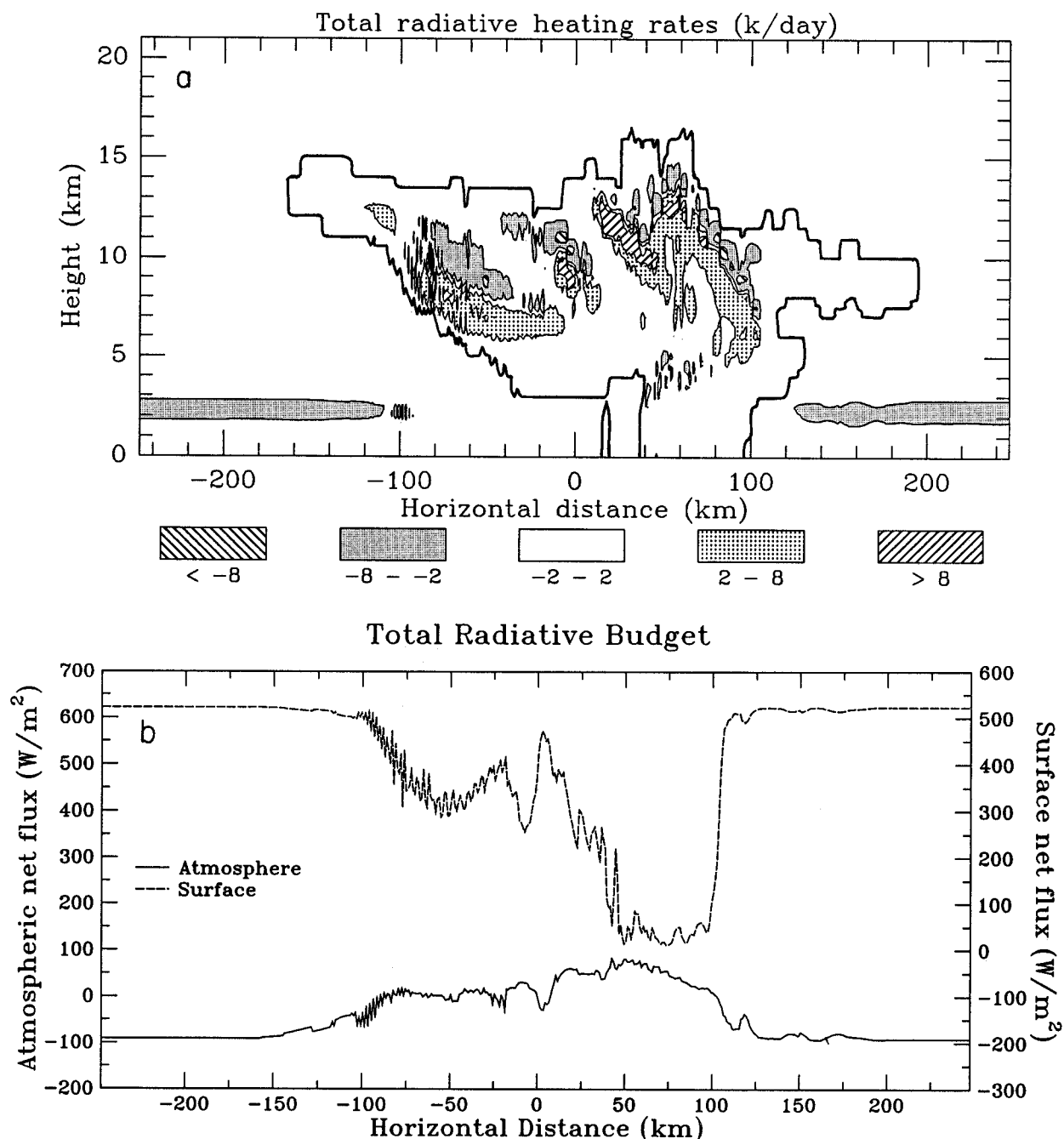

Fig. 8. Two-dimensional (X-Z) cross section of (a) total (short-wave plus infrared) radiative heating field (K/d) and (b) total radiative budgets (W/m²) as a function of the domain horizontal distance for the surface (dashed line and right label) and the atmosphere (solid line and left label) as diagnosed by the two-stream radiation model at 3 hours.

Clear sky region, Time = 3 hours

Thin anvil sky region, Time = 3 hours

Convective region, Time = 3 hours

Total cloud region, Time = 3 hours
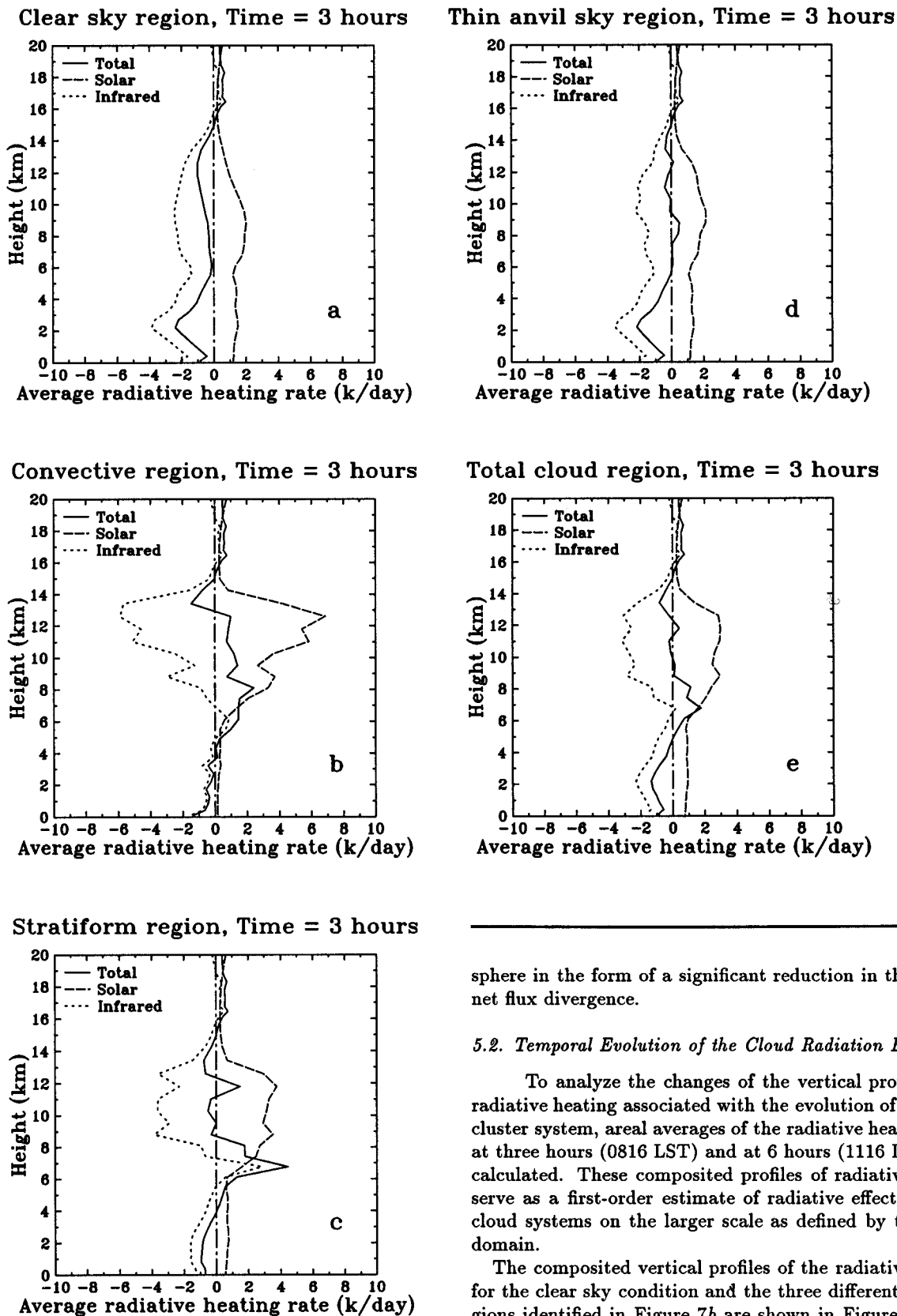

Stratiform region, Time = 3 hours

Fig. 9. Vertical profile of spectral radiative heating rate (K/d), including solar (dashed), infrared (dotted), and total (solid) for (a) the clear sky region, (b) the convective region, (c) the stratiform region, (d) the thin anvil region, and (e) the entire cloud cluster region at the simulation of 3 hours. The zero line (dashed-dotted) is also drawn in the figure for reference.

sphere in the form of a significant reduction in the column net flux divergence.

### 5.2. Temporal Evolution of the Cloud Radiation Budget

To analyze the changes of the vertical profile of the radiative heating associated with the evolution of the cloud cluster system, areal averages of the radiative heating fields at three hours (0816 LST) and at 6 hours (1116 LST) were calculated. These composited profiles of radiative heating serve as a first-order estimate of radiative effects of these cloud systems on the larger scale as defined by the model domain.

The composited vertical profiles of the radiative heating for the clear sky condition and the three different cloud regions identified in Figure 7b are shown in Figure 9 for the simulation time of 3 hours (0816 LST). The total (solar plus infrared) radiative heating profile in the clear sky region (Figure 9a) is predominantly one of cooling below 15 km and heating above this level due to the dominance of the infrared coolings over the clear sky solar heatings below 15 km. The profile in the convective region (Figure 9b) exhibits

a shallow cloud top cooling, a deep layer of in-cloud radiative heating, and a small radiative cooling below 3.5 km. The spectral breakdown of the radiative heating profile in this region shows that the heating rates occur as a small residual of the difference between the large infrared cooling rates and the large solar heating values. Comparisons between the clear sky profile (Figure 9a) and this profile show the significance of both in-cloud solar heating and in-cloud infrared cooling, especially near cloud top. The radiative profile corresponding to the stratiform region (Figure 9c) resembles that of the convective region. However, the deep layer of in-cloud radiative heating is interrupted by a layer of cooling in the stratiform region. A much stronger cloud base infrared heating also exists in this region. The spectral breakdown of this profile again emphasizes how the net heating is largely a result of the cancelling effects of long and shortwave radiation. The profile in the thin anvil region (Figure 9d) resembles that of the clear sky region with radiative cooling dominating the shape of the profile. The magnitude of the composite heating rates in the anvil region, relative to clear skies, does show both solar and infrared heating of the order of 1 K/d, indicating that the anvil region is radiatively heated by both solar and infrared radiation. The radiative heating profile averaged over the entire domain (Figure 9e) resembles the heating profile found in the stratiform region since the stratiform region contributes the majority of the area of the cloud cluster system. Comparisons between the clear sky profile in Figure 9a and this profile indicates how the cloud cluster leads to a systematic warming of the atmospheric column below 14 km.

The averaged profiles of the total radiative heating rate after 6 hours of simulation (1116 LST) are shown in Figures 10a, 10b, and 10c. Comparison of these clear sky profiles with those of Figure 9a shows how the solar heating has increased at this time, whereas the infrared heating remains similar to that calculated at 0816 LST. The total cloud system heating profile in Figure 10b exhibits a narrow region of cloud top total radiative cooling between 13 and 15 km and a deep layer of total radiative heating between 4 and 13 km. This total heating profile has a maximum in the upper troposphere about 2 to 3 km below the cloud top. Comparing these solar and infrared heating at this time shows how the strong cloud top infrared cooling is offset by the equally strong solar heating. It is also relevant to note how the solar heating is much stronger at this time (1116 LST) as well as weaker infrared cooling in the most of the cloud region except in the area near the cloud top, compared to the earlier simulation time. The cloud minus clear sky difference of radiative heating at 1116 LST (shown in Figure 10c), representing the radiative heating induced by the cloud cluster system, again shows that the net effect of the cloud system is to warm the atmosphere below cloud top. This radiative heating is governed by the infrared processes in the lower and middle troposphere and by solar heating in the upper troposphere. These figures, together with Figure 9 and Figure 2, further emphasize two important results of this study. Firstly, as local noon is approached, the effect of shortwave heating begins to dominate the heating profile of the cloud in the upper troposphere, as Figure 10c suggested. This is due to both the decreasing solar zenith angle and the increasing stratiform appearance of the cloud cluster system. Secondly, as the cloud cluster transforms to a stratiform system, the infrared heating in the lower and middle
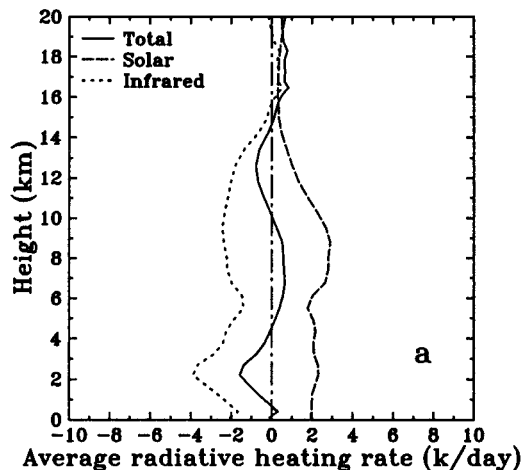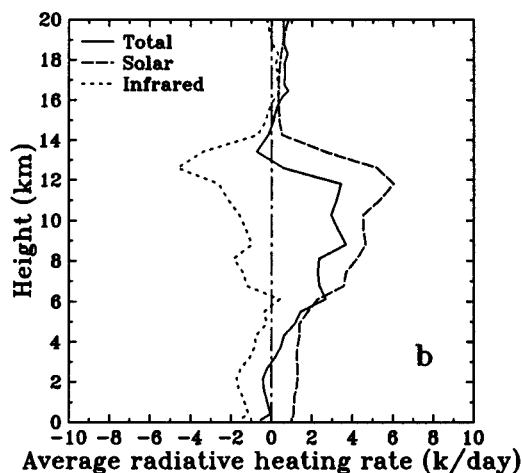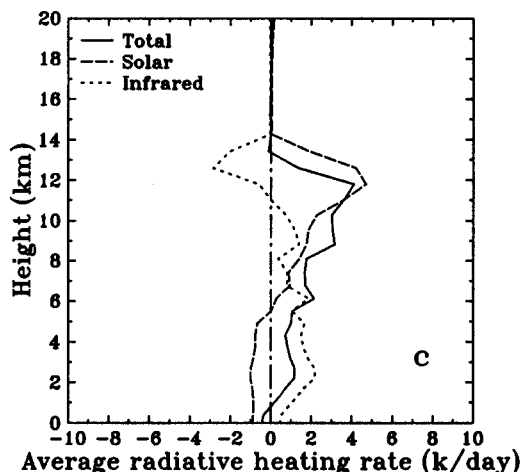

Fig. 10. The vertical profile of spectral radiative heating (K/d), including solar (dashed), infrared (dotted), and total (solid) for (a) the clear sky condition and (b) the cloud cluster system and (c) the difference between (b) and (a) for the simulation time of 6 hours. The zero line (dashed-dotted) is also drawn in the figure for reference.
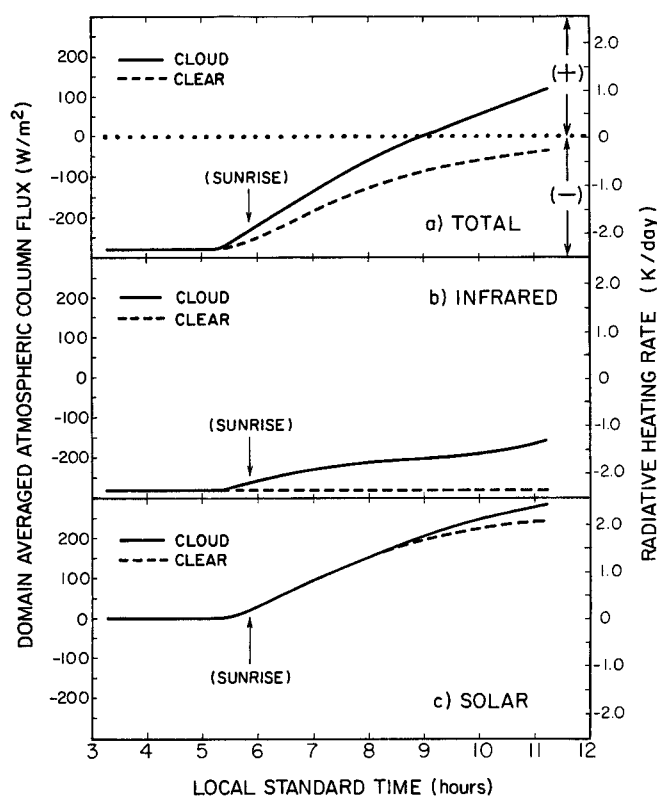
Fig. 11. Temporal change of domain-averaged atmospheric column radiative budget in W/m^2 (right label) and domain-averaged atmospheric column radiative heating field in K/d (left label) of the simulated cloud cluster case (solid) and of the simulated clear sky case (dashed) for (a) total radiation, (b) infrared radiation, and (c) solar radiation. The arrow in the figure indicates the time of sunrise. The cloud model is initialized at approximately 0516 LST.

troposphere strengthens due to the increased absorption of the infrared flux at cloud base.

The evolution of the domain-averaged atmospheric column flux divergence is shown in Figure 11 for the duration of the cloud simulation. The radiative fluxes were diagnosed every hour during this simulation and the results shown represent an average over the entire domain of the model. This atmospheric column flux represents the surplus/deficit of the radiative energy over the entire atmospheric vertical column and over the entire model horizontal domain. A positive value indicates that the atmosphere (containing both clear sky and cloud cluster) gains radiative energy and negative values correspond to loss of radiative energy. The evolution of the net solar, infrared, and total (solar plus infrared) flux divergences for the duration of the cloud simulation is shown on the left scale and as column-averaged heating rates on the right scale. Clear sky values are also included as a dashed line for comparison. The time scale is given on the x axis and spans from 0300 to 1200 LST. Sunrise is indicated on the diagram and the convection was triggered at about 0516 LST.

The net effect of the cloud cluster on the domain-averaged tropospheric radiation budget is clearly evident in this diagram. As the cloud system evolves (i.e., the fractional area covered by the cloud system in the model domain increases), the total radiative column flux divergence systematically increases from the clear sky minimum and becomes a positive

after 0900 LST. The difference between the clear sky and the cloudy sky total (solar plus infrared) fluxes is approximately 200 W/m^2 (or approximately 1.7 K/d) at the end of the model simulation (1116 LST). Of this 200 W/m^2, about 150 W/m^2 arise from infrared absorption primarily in the stratiform region of the cloud, while the remaining 50 W/m^2 are due to solar absorption in the atmosphere. As illustrated in Figure 10c, the solar heating effect, relative to clear sky, is concentrated in the upper troposphere, whereas the infrared heating, relative to clear sky, is found in the lower to middle troposphere. Figure 11 also shows how the solar heating varies systematically with the daily cycle of the Sun and exceeds the clear sky values only during the decaying phase of the system when the extensive stratiform cloud coincides with the low solar zenith angles. This indicates that both the effects of solar angle and the fractional cloud cover area are important in determining the total solar heating caused by these cloud systems. The infrared column flux divergence increases throughout the life cycle of the cloud system with the largest difference from the clear sky values also occurring during the latter stages of the life cycle when the model domain is covered by stratiform cloud and when the fractional area of cloud cover in the model is the largest. The more extensive is the stratiform cloudiness in the model domain, the greater is the reduction of longwave atmosphere column flux divergence. The results from this figure show how the tropical mesoscale cloud system provides an effective radiative heating source of the tropical atmosphere.

6. SUMMARY AND CONCLUSION

This paper describes an investigation which reports on calculations of the total (both solar and infrared) radiative heating distributions with a tropical MCS and the change of this heating through the life cycle of the cloud cluster. The approach used was to combine cloud modeling, radiation modeling, and analyses of observations obtained from the EMEX, the AMEX, and the STEP experiments.

The two-dimensional version of the Colorado State University regional atmospheric modeling system, initialized with data derived from both Darwin sounding and GMS satellite cloud motions, is used to simulate a tropical MCS. The broad features of the simulated MCS agree with those observed from the GMS satellite and the WP-3 aircraft. During its mature stage the modeled tropical cloud system had a maximum updraft of 4 m/s. The horizontal scale of the simulated MCS is of the order 40-50 km and 300-350 km for the convective and stratiform-anvil regions, respectively. The vertical scale of the simulated system is of the order 15 to 17 km. The convective area in the leading portion of the MCS has a rearward 16.5° sloping structure and seems to merge into the stratiform area. These are features similar to those obtained from observations reported in part 1. However, the simulated cloud cluster appears to move at a slower speed than the actual cloud system. The circulation of the simulated tropical MCS, consists of a low-level inflow into the leading convection, a low-level outflow behind this convection, an upper level outflow in front, and an upper level outflow behind of the system. The convective region consists of small cells of upward and downward motion with a horizontal scale of about 1-5 km. The location and the shape of the vertical motion field simulated by the cloud model are consistent with observations. A rear descending

inflow jet is also predicted in the stratiform region. Downward/upward motions are also observed inside/below the cloud deck in the anvil region. Strong horizontal wind shear exists near the cloud top and a low-level cold pool is evident behind the leading edge of the cloud boundary. Effects of subsidence warming also seem to be well simulated. The pressure perturbation field at the surface shows a mesohigh in the vicinity of the convection and a mesolow in the region to the rear of the system.

Radiation profiles are derived from a two-stream radiative transfer model using values from the model-simulated thermodynamic fields and hydrometeor mixing ratios. The results show how the atmosphere is significantly perturbed by the presence of the tropical MCS. The net effects of the MCS on the radiation budget are (1) the increase in the infrared emission to the surface and the decrease of the net infrared energy loss from the atmosphere relative to the clear sky emission. This reduction in the IR column net flux divergence may be as large as 150 W/m^2 in some areas of the cloud and is indicative of the significant greenhouse effect of these clouds. (2) Significant changes occur in the shortwave transmission to the surface, the shortwave albedo of the atmosphere, and the solar absorption in the atmosphere. The calculated low values of transmission in the convective region indicate how the MCS significantly reduces the solar flux to the surface relative to the clear sky values. (3) The vertical structure of the total radiative heating associated with the entire tropical MCSs is dominated by the heating profile in the stratiform region of the cloud system and the shortwave fluxes at the surface are most influenced by the deeper convective portions of the cloud. (4) The total radiative heating in the upper troposphere, especially near the cloud top region, is a result of the sensitive balance between the solar and the infrared heating in this region. The shortwave heating rate can be as large as the longwave cooling rate in this cloud top region, especially at local noon. The vertical structure of the radiative heating in the anvil region, on the other hand, shows heating by both solar and infrared radiation. (5) The net radiative effect of the tropical MCS, relative to the surrounding clear sky region, is a radiative heating of the atmosphere below the cloud top region through both solar and infrared heating and infrared cooling in a narrow area near the cloud top region. The vertical profile of this net heating also indicates the important of solar heating in the upper troposphere and infrared heating in the middle and lower troposphere.

The importance of the tropical cloud cluster systems on the radiative budget of the atmosphere is further emphasized by the evolution of the domain-averaged atmospheric column flux divergence for the duration of the MCS. As the cloud system evolves, the net column radiative energy loss of the atmosphere decreases and eventually becomes positive as the cloud system decays and transforms into a stratiform cloud system. This change in the column flux divergence translates into a total column radiative heating rate of approximately 1.7 K/d (relative to the clear sky radiative cooling rate). While the solar component of this total domain-averaged column heating is small and concentrated in the upper troposphere, the infrared contribution is spread over the lower and middle troposphere. The magnitude of this relative warming depends on the size of the stratiform area (i.e., cloud hydrometeor fields and fraction cloud area in the domain) and also on the solar zenith angle.

Whether these effects of radiation reported here play any role in evolution of the MCS itself is not known. The radiative heating may provide a significant forcing for the vertical motion in the upper troposphere, as suggested by *Dudhia* [1989]. The significant cloudy minus clear sky differences in the radiative heating that are reported throughout the evolution of the cloud cluster system of this study may also be important in sustaining the tropical convection by inducing a secondary circulation pattern, as proposed by *Gray and Jacobson* [1977]. Study of the basic feedback processes among dynamics, thermodynamics, microphysical, and radiative properties of these cloud systems will be the topic of a future study.

REFERENCES

Ackerman, T. P., K. -N. Liou, F. P. J. Valero, and L. Pfister, Heating rates in tropical anvils, *J. Atmos. Sci.*, *45*, 1606-1623, 1988.

Carlson, T., and J. Prospero, Saharan air outbreaks: Meteorology, aerosols, and radiation, in *Rep. of the U.S. GATE Cent. Program Workshop, Boulder, Colorado*, pp. 57-58, 1977.

Chen, C., and W. R. Cotton, A one-dimensional simulation of the stratocumulus-capped mixed layer, *Boundary Layer Meteorol.*, *25*, 289-321, 1983.

Chen, S., and W. R. Cotton, The sensitivity of a simulated extratropical mesoscale convective system to longwave radiation and ice-phase microphysics, *J. Atmos. Sci.*, *45*, 3897-3910, 1988.

Chong, M., P. Amayenc, G. Scialom, and J. Testud, A tropical squall line observed during the COPT81 experiment in West Africa, I, Kinematic structure inferred from dual-Doppler radar data, *Mon. Weather Rev.*, *115*, 670-694, 1987.

Chou, M.-D., Broadband water vapor transmission functions for atmospheric IR flux computations, *J. Atmos. Sci.*, *41*, 1775-1778, 1984.

Chou, M.-D., Parameterizations for the absorption of solar radiation by O_2 and CO_2 with application to climate studies, *J. Clim.*, *3*, 209-217, 1990.

Chou, M.-D., and A. Arking, Computation of infrared cooling rates in the water vapor bands, *J. Atmos. Sci.*, *37*, 855-867, 1980.

Chou, M.-D., and A. Arking, An efficient method for computing the absorption of solar radiation by water vapor, *J. Atmos. Sci.*, *38*, 798-807, 1981.

Chou, M.-D., and L. Peng, A parameterization of the absorption in the 15 μm spectral region with application to climate sensitivity studies, *J. Atmos. Sci.*, *40*, 2183-2192, 1983.

Cotton., W. R., and G. J. Tripoli, Cumulus convection in shear flow: Three dimensional numerical experiments, *J. Atmos. Sci.*, *35*, 1503-1521, 1978.

Cotton., W. R., M. A. Stephens, T. Nehrkorn, and G. J. Tripolie, The Colorado State University three-dimensional cloud/mesoscale model-1982, II, An ice parameterization, *J. Rech. Atmos.*, *16*, 295-320, 1982.

Cotton., W. R., G. J. Tripoli, and R. M. Rauber, Numerical simulation of the effects of varying ice crystal nucleation rates and aggregation processes on orographic snowfall, *J. Clim. Appl. Meteorol.*, *25*, 1658-1680, 1986.

Dudhia, J., Numerical study of convection observed during the Winter Monsoon Experiment using a mesoscale two-dimensional model, *J. Atmos. Sci.*, *46*, 3077-3109, 1989.

Gray, W. M., and R. W. Jacobson, Jr., Diurnal variation of

deep cumulus convection, *Mon. Weather Rev.*, *105*, 1171-1188, 1977.

Heymsfield, A. J., K. M. Miller, and J. D. Spinhirne, The October 27-28, 1986, FIRE IFO cirrus case study: Cloud microstructure, *Mon. Weather Rev.*, *118*, 2313-2328, 1990.

Houze, R. A., Jr., Observed structure of mesoscale convective systems and implications for large-scale heating, *Q. J. R. Meteorol. Soc.*, *115*, 425-461, 1989.

Houze, R. A., Jr., P. V. Hobbs, P. H. Herzegh, and D. B. Parson, Size distributions of precipitation particles in frontal clouds, *J. Atmos Sci.*, *36*, 156-162, 1979.

Houze, R.A., Jr., S.J. Bograd, and B. Mapes, An atlas of horizontal patterns of radar reflectivity observed during EMEX aircraft mission, *Dep. Atmos. Sci., Univ. of Washington, St. Louis, Mo.*, 1988.

Johnson, R. H., and P. J. Hamiltion, The relationship of surface pressure features to the precipitation and air flow structure of an intense midlatitude squall line, *Mon. Weather Rev.*, *116*, 1444-1472, 1988.

Klemp, J. B., and D. K. Lilly, Numerical simulation of hydrostatic mountain waves, *J. Atmos. Sci.*, *35* 78-107, 1978.

Kneizys, F. X., E. P. Shettle, W. O. Gallery, J. H. Chetwynd, Jr., L. W. Abreu, J. E. A. Selby, R. W. Fenn, and R. A. McClatchey, Atmospheric transmittance/radiance: Computer code LOWTRAN 5, AFGL Tech. Rep. *AFGL-TR-80-0067*, 200 pp., 1980.

Leary, C. A., and R. A. Houze, Jr., Melting and evaporation of hydrometeors in precipitation from the anvil clouds of deep tropical cumulonimbus anvils, *Geophys. Res. Lett.*, *6*, 613-616, 1979.

Lilly, D. K., Cirrus outflow dynamics, *J. Atmos. Sci.*, *45*, 1594-1605, 1988.

Moncrieff, M. W., and M. J. Miller, The dynamics and simulation of tropical cumulonimbus and squall lines. *Q. J. R. Meteorol. Soc.*, *102*, 373-394, 1976.

Nicholls, M. E., A comparison of the results of a two-dimensional numerical simulation of a tropical squall line with observations, *Mon. Weather Rev.*, *115*, 3055-3077, 1987.

Nicholls, M. E., and M. J. Weissbluth, A comparison of two-dimensional and quasi-three-dimensional simulations of a tropical squall line, *Mon. Weather Rev.*, *116*, 2437-2452, 1988.

Paltridge, G. W., and C. M. R. Platt, *Radiative Processes in Meteorology and Climatology*, 318 pp., Elsevier, Amsterdam, 1976.

Ramanathan, V., and W. Collins, Thermodynamic regulation of ocean warming by cirrus clouds detected from observations of the 1987 El Nino, *Nature*, *37-6321*, 27-32, 1991.

Stackhouse, P. W., Jr., and G. L. Stephens, A theoretical and observational study of the radiative properties of cirrus: Results from FIRE 1986, *J. Atmos. Sci.*, *48*, 2044-2059, 1991.

Stephens, G. L., Radiative properties of extended water cloud, II, Parameterization, *J. Atmos. Sci.*, *35*, 2123-2132, 1978.

Stephens, G. L., and T. J. Greenwald, The earth's radiation budget and its relation to atmospheric hydrology, 2, Observation of cloud effects, *J. Geophys. Res.*, *96*, 15,325-15,340, 1991.

Stuhlmann, R., and G. L. Smith, A study of cloud-generated radiative heating and its generation of available potential energy, I, Theoretical background, *J. Atmos. Sci.*, *45*, 3911-3927, 1988a.

Stuhlmann, R., and G. L. Smith, A study of cloud-generated radiative heating and its generation of available potential energy, II, Results for a climatological zonal mean January, *J. Atmos. Sci.*, *45*, 3928-3943, 1988b.

Tao, W.-K., J. Simpson, and S.-T. Soong, Statistical properties of a cloud ensemble: A numerical study, *J. Atmos. Sci.*, *44*, 3175-3187, 1987.

Thorpe, A. J.,, M. J. Miller, and M. W. Moncrieff, Two-dimensional convection in non-constant shear: A model of mid-latitude squall lines, *Q. J. R. Meteorol. Soc.*, *108*, 739-762, 1982.

Tripoli, G. J., and W. R. Cotton, A numerical investigation of several factors contribution to the observed variable intensity of deep convection over Florida, *J. Appl. Meteorol.*, *19*, 1037-1063, 1980.

Tripoli, G., J., and W. R. Cotton, The use of ice-liquid water potential temperature as a thermodynamic variable in deep atmospheric models, *Mon. Weather Rev.*, *109*, 1094-1102, 1981.

Tripoli, G., J., and W. R. Cotton, The Colorado State University three-dimensional cloud mesoscale model-1982, I, General theoretical framework and sensitivity experiments, *J. Rech. Atmos.*, *16*, 185-220, 1982.

Webster, P. J., and R. A. Houze, The Equatorial Mesoscale Experiment (EMEX): An overview, *Bull. Am. Meteorol. Soc.*, *72*, 1481-1505, 1991.

Webster, P. J., and G. L. Stephens, Tropical upper-tropospheric extended clouds: Inferences from winter MONEX, *J. Atmos. Sci.*, *37*, 1521-1541, 1980.

Wong, T., G. L. Stephens, P. W. Stackhouse, Jr., and F. P. J. Valero, The radiative budgets of a tropical mesoscale convective system during EMEX-STEP-AMEX Experiment, 1, Observations, *J. Geophys. Res.*, this issue.

Xu, K.-M., and S. K. Krueger, Evaluation of cloudiness parameterizations using a cumulus ensemble model, *Mon. Weather Rev.*, *119*, 342-367, 1991.

T. Wong, G. L. Stephens and P. W. Stackhouse, Jr., Department of Atmoshperic Science, Colorado State University, Ft. Collins, CO 80523.

F. P. J. Valero, NASA AMES Research Center, Moffett Field, CA 94035.